www.sciencemag.org/content/344/6186/877/suppl/DC1

Supplementary Material for

Disproportionation of (Mg,Fe)SiO_3 perovskite in Earth's deep lower mantle

Li Zhang,* Yue Meng, Wenge Yang, Lin Wang, Wendy L. Mao, Qiao-Shi Zeng, Jong Seok Jeong, Andrew J. Wagner, K. Andre Mkhoyan, Wenjun Liu, Ruqing Xu, Ho-kwang Mao

*Corresponding author. E-mail: zhangli@hpstar.ac.cn

Published 23 May 2014, *Science* **344**, 877 (2014)
DOI: 10.1126/science.1250274

This PDF file includes:

Materials and Methods

Starting materials

The starting samples used in this study include: orthopyroxene (opx) samples with the compositions of $(Mg_{0.85}Fe_{0.15})SiO_3$ (Fs15) and $(Mg_{0.60}Fe_{0.40})SiO_3$ (Fs40); Al_2O_3 bearing opx with composition $(Mg_{0.80}Fe_{0.20})(Al_{0.04}Si_{0.96})O_3$; perovskite (pv) structured $(Mg_{0.90}Fe_{0.10})SiO_3$ (pv10); another sample with excess (Mg,Fe)O with the composition of $MgO:FeO:SiO_2=0.86 : 0.19 : 1.0$, leading to $(Mg,Fe)SiO_3$:(Mg,Fe)O =20:1 in the system. The compositions of these samples and their implied oxygen fugacities are directly relevant to the Earth's mantle (*29, 30*).

Following the well-established synthesis procedure described in earlier studies (*31*), the starting oxide mixtures were prepared by weighing MgO, Fe_2O_3, and SiO_2 with required proportions, with slightly excess SiO_2 to avoid the formation of Fe-bearing phase in addition to opx. The mixtures were ground in acetone in an agate mortar for one hour to ensure homogeneity. The oxide mixtures were dried and loaded in a Pt crucible and reacted in a CO_2–CO gas-mixing furnace at 1473 K and oxygen fugacity (fO_2) of $10^{-10.5}$ for 24 hours to reduce all Fe^{3+} to Fe^{2+}. The treated mixtures were reground and sealed in a graphite capsule, which were then compressed in a piston-cylinder apparatus for 48 hours at 1623 K and 1.2 GPa. Electron microprobe and x-ray diffraction (XRD) analyses of the products confirmed the stoichiometric opx compositions with the intended Fe/Mg ratios along with small amount of evenly distributed SiO_2 as an additional inert component.

The details of the pre-synthesized $(Mg_{0.90}Fe_{0.10})SiO_3$ pv (pv10) sample in a multianvil press were described elsewhere (*14, 24*) and the pv10 sample is from the same batch that has been used in previous studies (*6, 25*).

Sample loading and compression

Each of the starting materials was loaded in a Mao-type symmetric diamond anvil cell (DAC) separately for high pressure-temperature (*P*-*T*) experiments. Diamond anvils with flat culet diameters of 150 μm beveled at 10° up to 300 μm were mounted in Boehler seats with up to 60° x-ray opening.

The sample was pre-compressed into disks of ~10 μm thickness and cut to 40-60 μm in diameter and placed in a rhenium (Re) gasket hole with diameter ~60 μm filled with Ne, NaCl, or SiO_2 glass as both pressure transmitting media and thermal insulating layers during laser-heating. We paid special attention to experimental details and noticed the improvement of the data quality by improving the experimental details. To achieve the best possible data quality, we have also tested different loadings and optimized the heating by controlling the initial thickness of both sample and gasket and managed to sandwich the sample between symmetric insulation layers of Ne or solid media from both sides. Our opx sample was prepared by compressing a single crystal and thus sample homogeneity was ensured.

X-ray diffraction (XRD) measurements were conducted at the high-pressure synchrotron

beamlines 16ID-B and 13ID-D, and the micro-XRD beamline 34ID-E of the Advanced Photon Source (APS), Argonne National Laboratory. The double-sided on-line YLF laser-heating system was used to create a relatively large heating area (30-50 μm) with a flat temperature distribution on the sample. The incident x-ray beam was focused to 6×8 μm^2 spot impinging upon the sample, and XRD patterns of the sample were collected with a MAR165 CCD detector *in-situ* at high *P-T* and after-quenching to ambient *T* and high *P* conditions. The pressure was determined from the unit cell volumes of the pressure media Ne, NaCl or SiO_2 calibrated with Ne (*32*). Thick insulation layers from both sides and a large heating spot with a flat temperature distribution promoted phase equilibrium in the system, as evident by a typical XRD pattern (Fig. S1) where the diffraction peaks of the Ne medium are several times stronger than the peaks from the silicate at 96 GPa and 2300 K. The intensities of the Ne peaks were trimmed to show details of the sample peaks as shown in Fig. 1A.

Laser heated *in-situ* high-pressure x-ray diffraction

Most of our experiments were performed at HPCAT. The micro-focused x-ray diffraction with *in-situ* laser heating provides the following capabilities including but not limited to: (1) Undulator-based angle-dispersive monochromatic XRD with micro-focused beam ~ 5 to 8 μm; (2) X-ray energy range 12 to 42 KeV; (3) Double-sided heating of DAC with two100W YLF fiber lasers; (4) Separate temperature measurements from both sides; (5) Temperature measurement with an imaging spectrograph and a PIXIS 400BR CCD detector. New capabilities established in recent years includes (1) *in-situ* heating spot variation (flat top area 4 to > 60 μm, FWHM 9 to > 120 μm) to provide effective and uniform heating on various sample sizes in a diamond anvil cell (designed and made by HPCAT in collaboration with Reinhard Boehler); (2) mirror pinhole setup to allow experimenters to directly observe the spectrograph pinhole position, where the temperature sampling area is defined in temperature measurement, relative to the heating spot and x-ray position and to make adjustment if needed.

We have learned through many experiments in the past two years that sample environment is important for the synthesis of the H-phase. For instance, we found the H-phase grows more readily in Ne medium which provides a quasi-hydrostatic environment superior than other media. Although experimentally Ne is more difficult to handle than solid media, we conducted most of our experiments in the Ne medium. The relative intensity of the Ne111 peak is about 5 times higher than the strongest peak of the pv phase (Fig. S1), indicating that our samples were well insulated during the heating. The high Ne/sample ratio is a unique feature in our experiments. Note the disproportionation could occur within 2 minutes' heating in such an environment, because hydrostaticity and stable heating create a perfect environment for phase equilibrium at high *P*. We have successfully repeated the observation of the disproportionation in the environment of both NaCl and SiO_2 glass to ensure the chemical inertness of Ne with our investigated system. Very stable and uniform heating above 2200 K with longer heating duration was required to observe the disproportionation with good quality in these less hydrostatic environments. The heating quality is determined by the uniformity in a relatively large heating spot and the temperature stability during the heating, as demonstrated in Fig. S2 and Fig. S3. The diameter of the spot size is ~50 μm with a flat temperature distribution

covering ~90% sample area; the power loss is controlled to a minimum using excellent insulation; the temperature is maintained within ±50 K fluctuation and this kind of environment is superior for phase equilibrium as evident by the fully developed coarse-grained pv phase and H-phase.

Multigrain crystallography

The powder XRD data analysis program DICVOL06 (*33*) yielded a hexagonal unit cell for the H-phase, however, powder XRD patterns contain *d*-spacing information and indexing match of multiple peaks could still be non-unique. Single-crystal Bragg reflection spots, on the other hand, provide rigorous 3-dimensional angular and symmetry relations in addition to the *d*-spacings, thus unequivocally constraining the unit cell parameters. Single-crystal Bragg reflection spots, on the other hand, provide rigorous 3-dimensional angular and symmetry relations in addition to the *d*-spacings, thus unequivocally constraining the unit cell parameters. The highly spotty XRD patterns require a new analytical approach. Our goal was to index individual crystallites in a polycrystalline sample through determination of orientation matrix for each crystallite.

We aligned the sample to the ω-rotation center and collected a complete set of two-dimensional multiple-crystal XRD patterns at ω increment of 0.1° over the range of -21° to 21°, similar to the "rotation method" used in conventional single-crystal crystallography. The software package named Fully Automatic Beamline Experiments (FABLE) (*22*) was used to determine crystallographic orientations of individual crystallites in this study. This indexing procedure that has been well demonstrated for high-pressure DAC data (*34*). The monochromatic x-ray beam available at HPCAT is brilliant enough to record individual diffraction spots from hundreds of submicron crystallites in a coarse-grained polycrystalline sample. The indexing procedure was carried out using the program *GrainSpotter* in the FABLE package (*22*), which takes as input a list of measured scattering vectors in reciprocal space and a list of theoretical scattering vectors derived from the lattice parameters and space group. The algorithm determines individual crystallographic orientations through finding replicas of the set of theoretical scattering vectors in the measured dataset.

The main limitation for indexing orientations is overlap of diffraction spots originated from many different crystallites in each diffraction pattern. In this study, when small rotation steps are used to record individual diffraction patterns, most of the diffraction spots can be treated individually without overlapping with those from neighboring spots in one XRD pattern. A unique orientation matrix for each crystallite was indentified when multiple spots were shown to originate from a single orientation, and indeed these spots were confirmed within the predicted diffraction angles (ω, 2θ, and η), where ω, θ, and η represent the rotation, Bragg, and azimuth angles, respectively. The matrix of each crystallite was then optimized. Within the beam size of 6×8 μm^2 at 101 GPa, 154 individual crystallites, each with 11 to 27 reflections consistent with the new H phase, were identified. Meanwhile, 130 individual crystallites of the coexisting pv phase were also identified at the same beam position.

With the multigrain XRD software identifying orientation matrices for over one hundred of H-phase single crystallites, and each matrix locating dozens of single-crystal XRD spots, the unit cell parameters of the H-phase have been well established. In principle, the intensity information such as Tables S1 and S2, should be sufficient for us to solve the crystal structure and define all atomic positions. However, possible structures with the small Z=2 unit cell had unusually short Si-Si bond or too high enthalpy. More likely the small unit cell is a sub-unit of a (n times) superlattice with Z=2n. We have made a great deal of effort searching for the very weak superlattice XRD spots, and significantly more time may be needed. Here, we presented the intensity data in Table S1 and S2 for H-phase single crystallites that would allow a community effort to attempt a structure solution.

Post-experimental *ex-situ* FIB sample preparation and STEM-EDX analysis

The experimental products from the $(Mg_{0.85}Fe_{0.15})SiO_3$ (Fs15) starting material were synthesized at 101 GPa and 2200-2400 K in a Ne medium and subsequently decompressed (Fig. 1C) and recovered to ambient conditions (Fig. 1D) for *ex-situ* transmission electron microscopy (TEM) study. An FEI Quanta 200 3D focused ion beam (FIB) instrument was used for the preparation of TEM specimens. A lamella of approximately $20\times5\times2$ μm^3 was cut by FIB from the center potion of the laser heated spot in the recovered sample. The lamella was attached to a tungsten needle by platinum welding and lifted out with an Omniprobe (Fig. S5(A)). The lamella was then welded to a Cu grid and further thinned to ~200 nm for TEM analysis (Fig. S5(B)). The bright-field (BF) and annular dark-field (ADF) scanning transmission electron microscopy (STEM) images were obtained using a FEI Tecnai G2 F30 S-TEM equipped with an energy dispersive x-ray (EDX) spectrometer operated at accelerating voltage of 300 kV. The STEM has semi-convergent angle of 9 mrad and ADF detector inner angle of 31 mrad. The EDX mapping with a size of 100×50 $pixel^2$ was performed at a scanning rate of 500 ms/pixel with drift correction. Each individual EDX spectrum was collected for 60 s.

The sample section demonstrated both compositional and phase heterogeneities. To explore the nature of the heterogeneities and their correlation to the *in-situ* XRD data, we performed STEM-EDX mapping, compositional analysis, and selected area electron diffraction (SAED) for each phase (Fig. S6). The EDX data suggested that $MgSiO_3$ is the dominant phase in position 1 (Fig. S6(K)) and the BF image and SAED pattern indicate that the phase is well crystallized (Fig. S6(A) and (G)), confirming the Fe-depletion in the pv phase. A small piece of crystalline SiO_2 was found in the position 2 (Fig. S6(H) and (L)), consistent in quenchable structure and overall quantity with the excess SiO_2 in the starting composition and the *in-situ* XRD observations. Unlike the quenchable crystalline $MgSiO_3$ pv, the ultrahigh-pressure H phase is highly unstable at ambient conditions and further decomposed during the sample preparation process for STEM (Fig. S6(I-J, M-N)), so its properties must be studied *in-situ* at high pressures. The SAED patterns show that the iron-oxide rich phase in position 3 is crystallized (Fig. S6(E), (I), and (M)) and the iron-free phase in the neighboring position 4 is amorphous (Fig. S6(J)). Nevertheless, the integrated composition of the iron-oxide crystals and the coexisting amorphous phase is close to the Fe-rich $(Mg,Fe)SiO_3$.

Supplementary Text

Reversal of the disproportionation

We repeated the Fs15 composition with Ne pressure medium and again observed the disproportionation reaction and formation of the new H phase at 103 GPa. We gradually decompressed the sample, performed laser heating and monitored the changes of both the pv and H phases. When the pressure was released to 95 GPa and heated to 2000K, the H phase was unchanged (Fig. S7(A)). When the pressure was released to 67GPa and heated to 2000 K, the H phase clearly diminishes and only the pv peaks remained (Fig. S7(B)).

Full profile fit of integrated high-pressure powder x-ray diffraction spectra

We have applied the general structural analysis system (GSAS) for the full spectra corresponding to the sample shown in Fig. 2 (Fig. S8). The peak positions (d-spacings) fit the H-phase extremely well. The full profile analysis demonstrates that the marked peak positions are correct and correspond to the lattice parameters as indicated by the symmetrical residual peaks, consistent with the good fit between the calculated and observed values in Table1. We often obtained very spotty XRD patterns due to crystal growth to submicron-sized crystal aggregate at high T within the 6×8 μm^2 x-ray beam spot. The peak position analysis is valid and provides decisive confirmation of the lattice parameters of the H-phase, but the peak intensities are largely affected by the presence or absence of strong spots. As we can see, even the well-known fcc neon shows large positive and negative residual intensities.

The challenge of discovering the disproportionation and H phase

Unlike the pv or ppv that can form a single phase and produce a distinctive set of powder XRD peaks after transition, the H phase as a disproportionation product produces a couple of secondary peaks in the predominant pv powder XRD pattern. With powder XRD alone, the H phase would be hard to discover and easy to miss in comparison to pv or ppv. These new peaks at 2.55 and 2.40Å can also be confused with (although do not exactly fit) the ppv pattern. Discovery of H phase based on these two powder peaks alone would be less than convincing; only by using the multigrain single-crystallite method can the H phase be delineated from the pv and clearly identified beyond doubt.

Moreover, our experiments demonstrated that the H phase can only be synthesized at temperatures above 2200 K and earlier experiments, performed under 2000 K, would not have produced the H phase. Two years ago, we noticed the weak 2.55 and 2.40Å peaks together with a much weaker 4.41Å peaks which is $\sqrt{3}$ times 2.55, suggesting a hexagonal unit cell (Fig. S9 shows a pattern with weak H peaks). We conducted an in-depth investigation, but the results were not always reproducible; sometimes the H phase was present, sometimes not or very weak. After many experiments, we learned the followings:

1. The H phase did not grow below 2000 K.
2. Even the average temperature was above 2200 K, the H phase did not grow well unless we had a perfect heating condition, *i.e.*, stable heating without flashing, large uniform heating spot with minimal Fe diffusion, constant T from both side of the DAC, etc.

3. The H phase grew faster and better if we went directly from the metastable compressed opx to 2300 K rather than converting a well crystallized pv to H phase.
4. When the H phase was abundant and grew well, the coexisting pv showed a smaller unit cell corresponding to the pure $MgSiO_3$.

The devil is in the detail, and now by obtaining the appropriate conditions, we observed the disproportionation repeatedly. In addition to paying great attention to the common prerequisites, such as the purity and uniformity of the starting samples and pressure media, removing surface moisture, preparing a perfectly centered sample chambers, preparing sample platelets with uniform thickness and symmetric insulation layers, etc., we have a number of unique advantages to obtain the observations.

(1) Thick insulation layers (Fig. S1), large heating spot (~50 μm with a flat temperature distribution over the whole sample area) and the stable and uniform heating (±50 K over time) (Fig. S3), are all important factors. They provide a superior heating environment for the disproportionation and for phase equilibrium as evident by fully developed coarse-grained pv and H phases.
(2) We were able to track the quenchability of the Fe-depleted pv and disappearance of the H phase all the way down to ambient conditions (Fig. 1C) with XRD during the decompression. High quality *in-situ* XRD patterns, and *ex-situ* STEM diffraction and composition analysis provide clear evidences for the preservation of the Fe-depleted pv phase at ambient conditions and the disproportionation at high *P-T*.
(3) The H-phase often appears as spotty patterns. The newly developed multigrain single-crystallite method is invaluable to establish the primary unit cell and symmetry of such spotty patterns at Megabra pressure.
(4) During the past two years, we have devoted a total of 130 shifts of synchrotron beam time at four facilities for this project. Such concentration of beam time and efforts for a single project within this limited *P-T-x* system is necessary for pinning down this challenging observation.

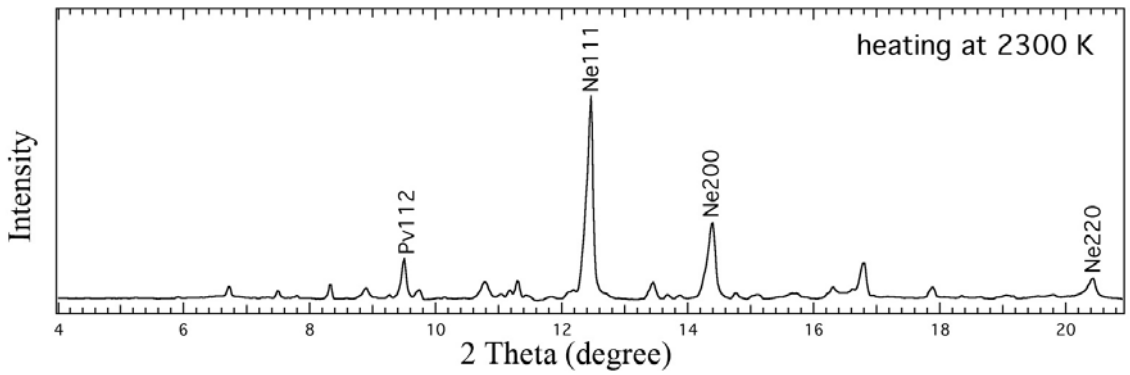

Fig. S1 A representative full intensity XRD pattern in Ne medium. The Ne peaks are several times more intense than those of the pv.

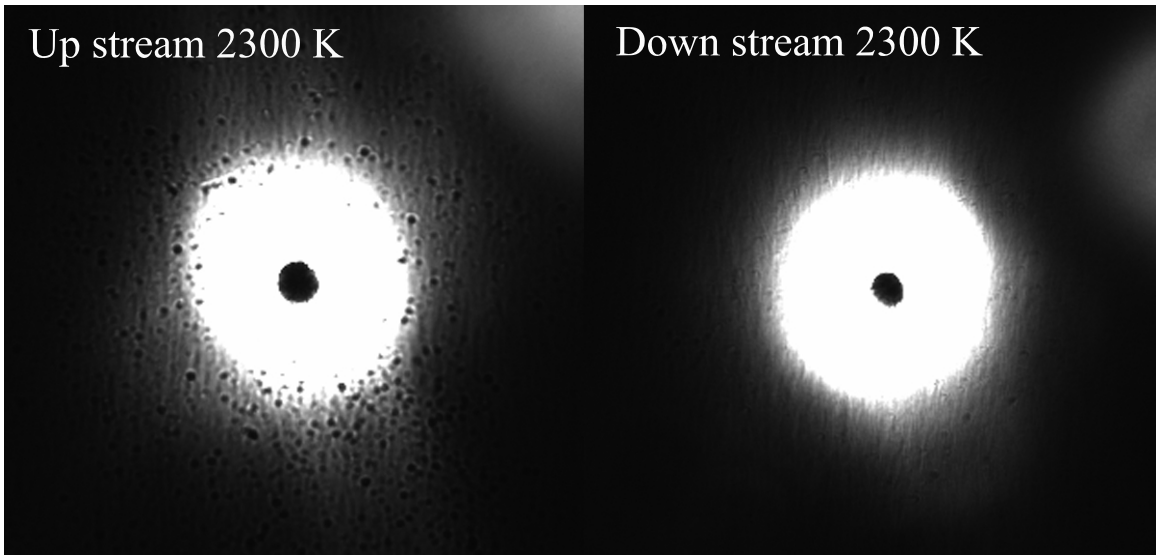

Fig. S2 Heating spots from double side heating. The temperatures of both sides were measured to be ~2300 K on the sample sandwiched between SiO_2 layers at 101 GPa. The diameter of the spot size is ~50 μm with a flat temperature distribution on the sample.

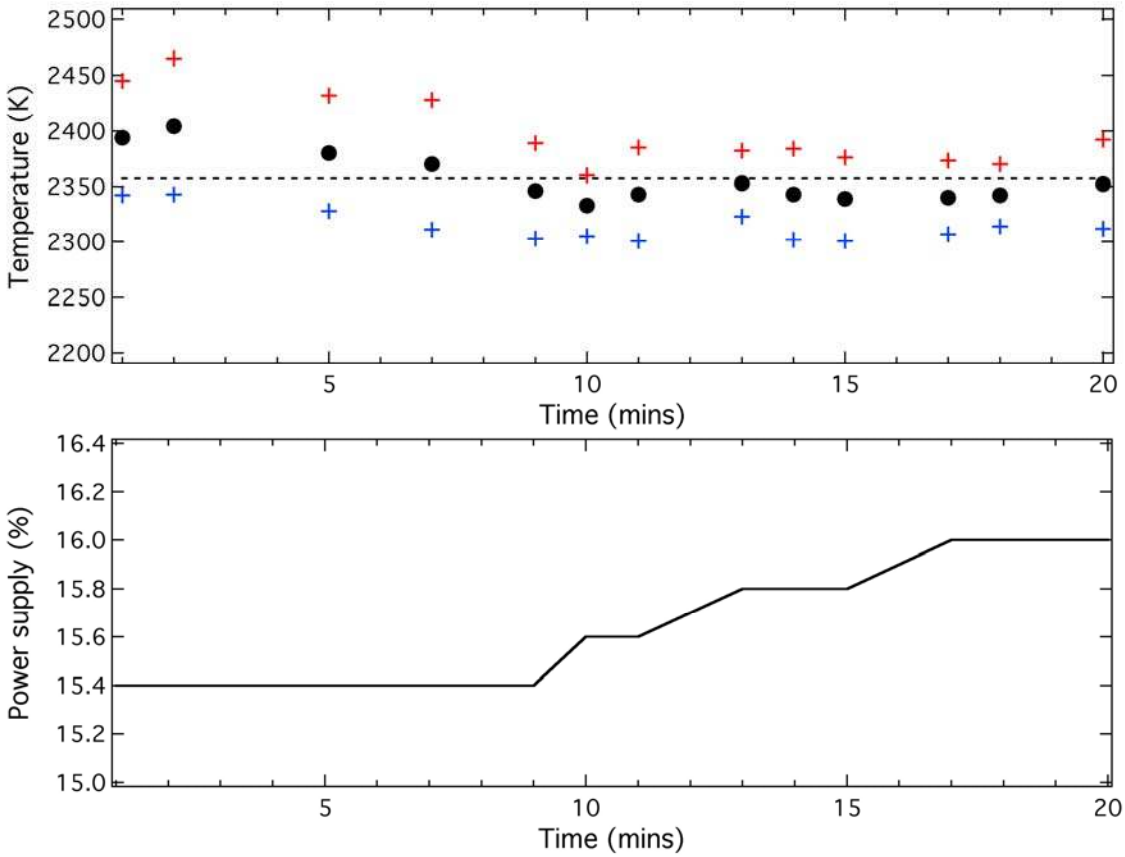

Fig. S3 Temperature stability during heating. Measured temperatures and power supplies from both sides are plotted with time when the sample was heated in SiO_2 glass medium at 100 GPa. In the up figure, the blue and red crosses represent the temperatures from up stream and down stream, respectively. The black solid circles and dashed line represent the average temperature from both sides and average temperature through the 20 minutes' heating, respectively. The bottom figure shows the corresponding power supply for each side during the heating.

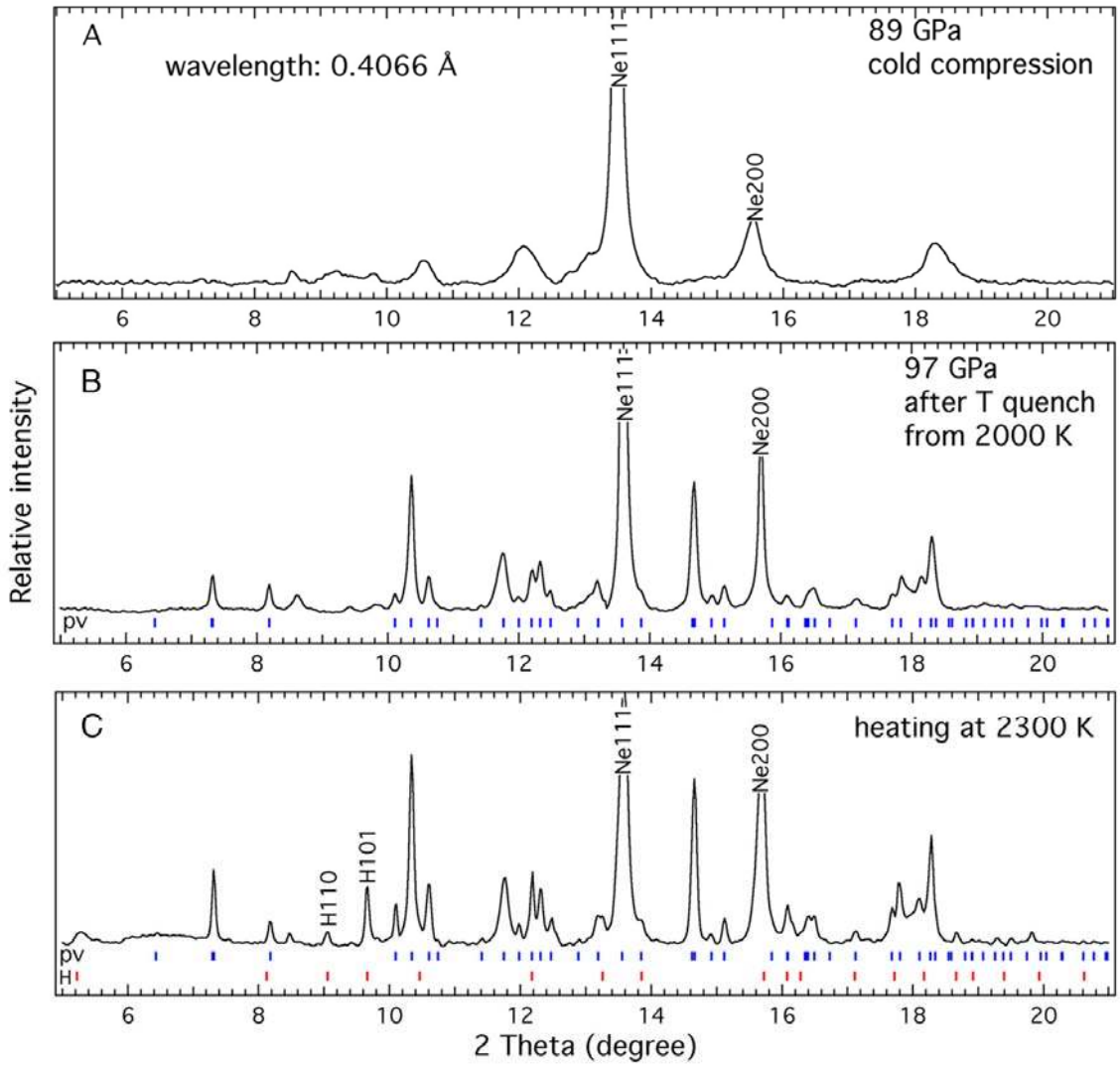

Fig. S4 *In-situ* powder XRD patterns of Fs15 in a Ne medium. Compressed to 89 GPa at 300K (A); T quench to 300 K from heating at 2000 K, 97 GPa (B); appearance of H-phase with further heating at 2300 K (C).

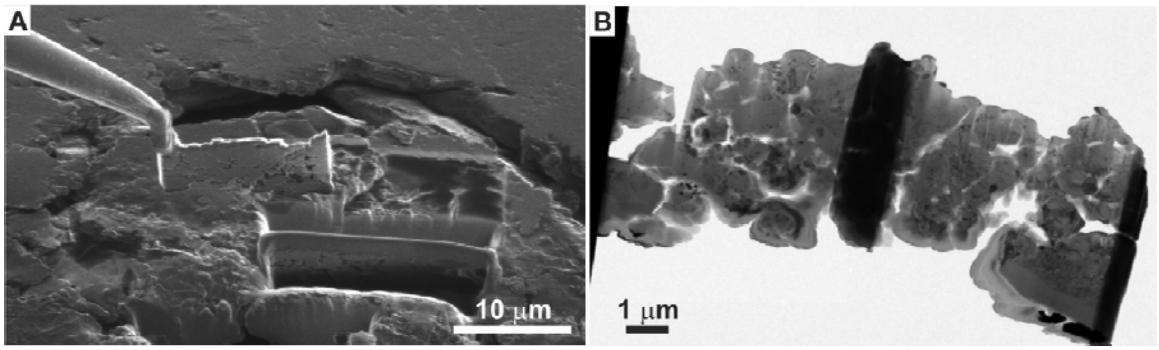

Fig. S5 A TEM specimen prepared by the FIB. (A) Lift-out of a lamella using an Omniprobe and (B) conventional TEM-BF image of the specimen.

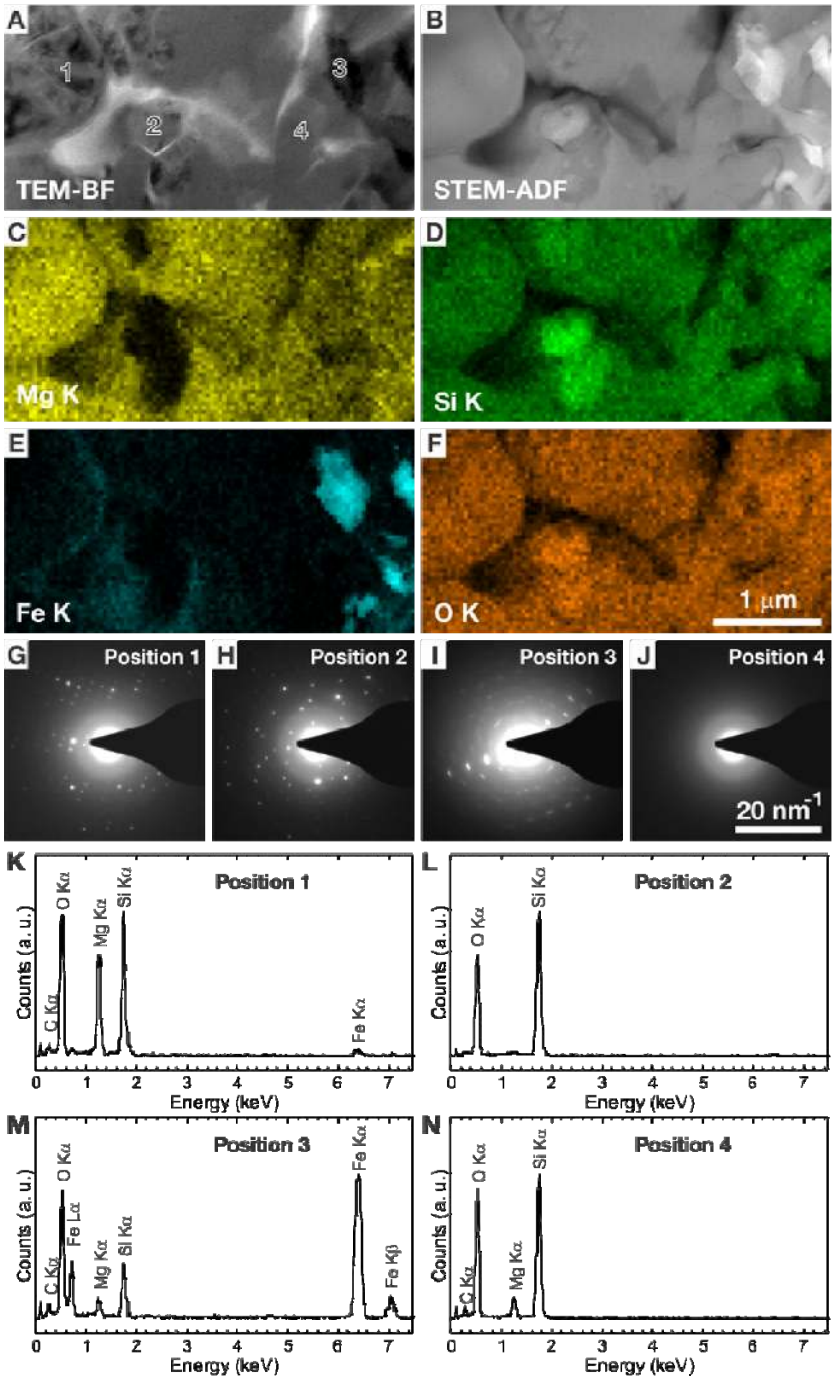

Fig. S6 STEM-EDX analysis of the recovered products. (A) TEM-BF image, (B) STEM-ADF image and (C-F) corresponding STEM-EDX maps—(C) Mg K, (D) Si K, (E) Fe K, and (F) O K—are presented. STEM-ADF and EDX maps were obtained simultaneously. (G-J) SAED patterns and (K-N) EDX spectra were also obtained from the positions indicated in (A).

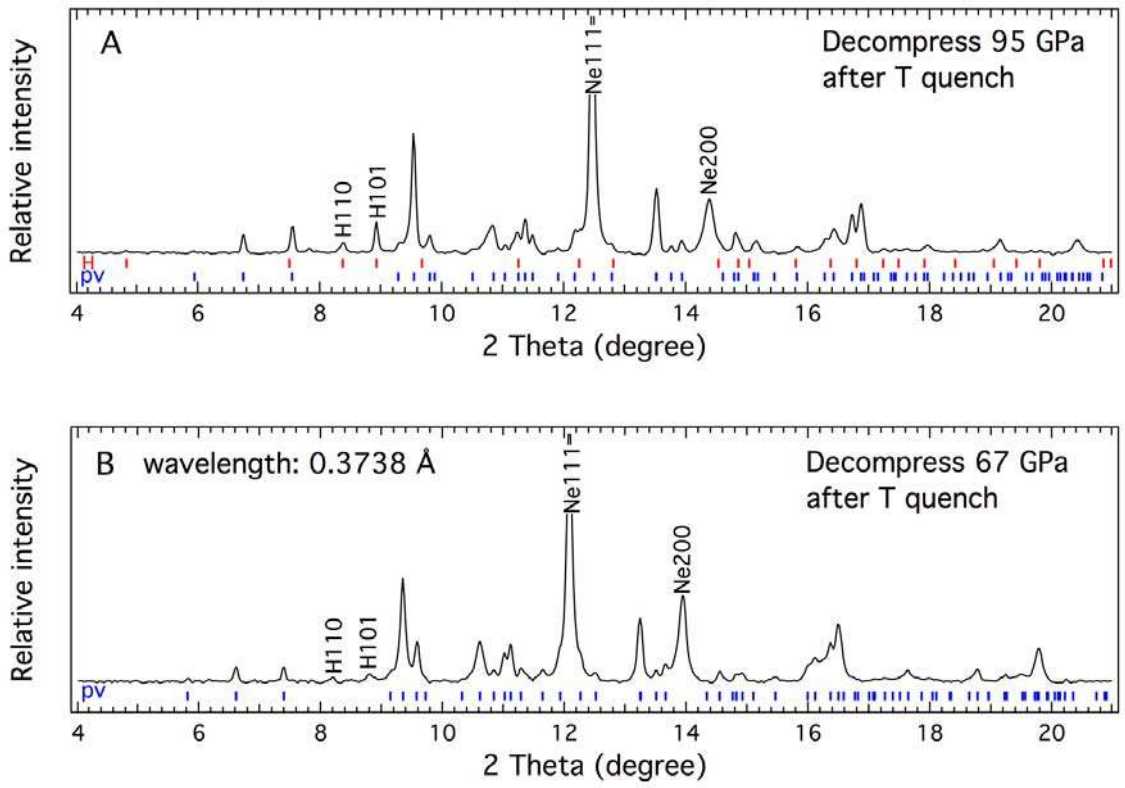

Fig. S7 The reversal experiment. (A) XRD pattern of run products at 95 GPa after *T* quench to 300 K from heating at 2000 K; (B) Disappearance of the H phase from heating at 2000 K and 67 GPa (pressure measured after *T* quench).

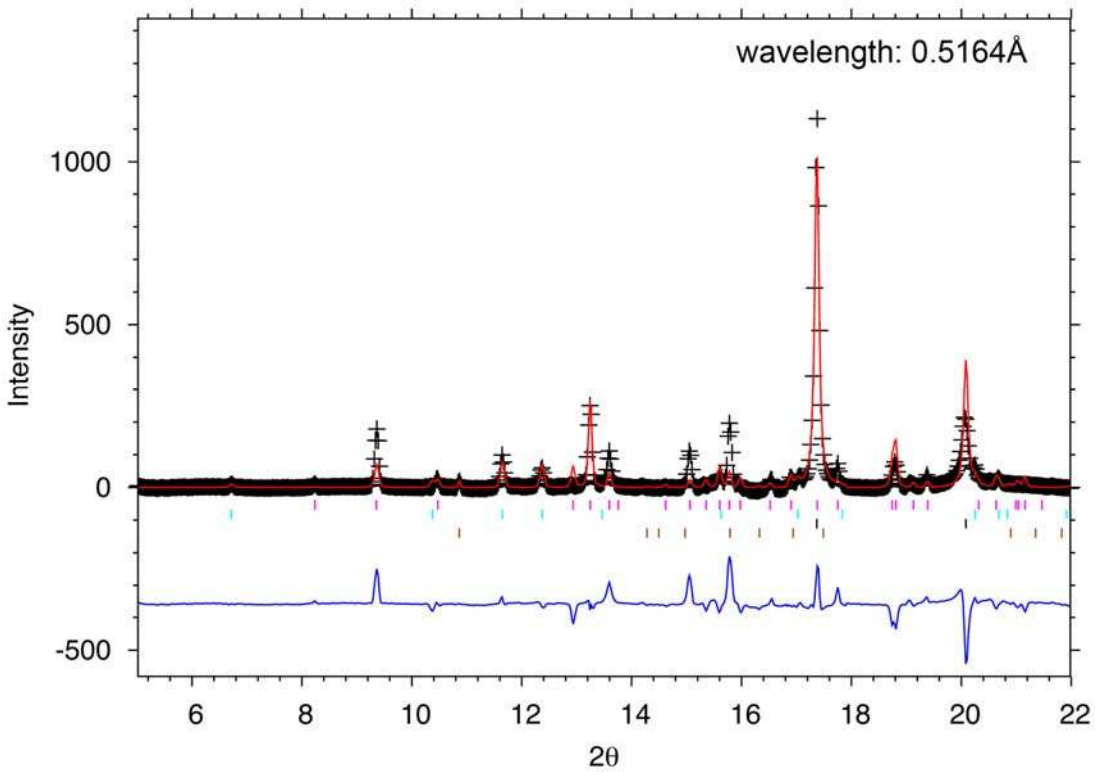

Fig. S8 The GSAS plot. Black pluses are the experimental data, the red curve is the simulated diffraction pattern and the blue line represents the residual differences. The tick-markers from top to bottom correspond to pv, H, Ne and SiO_2 ($CaCl_2$ structure).

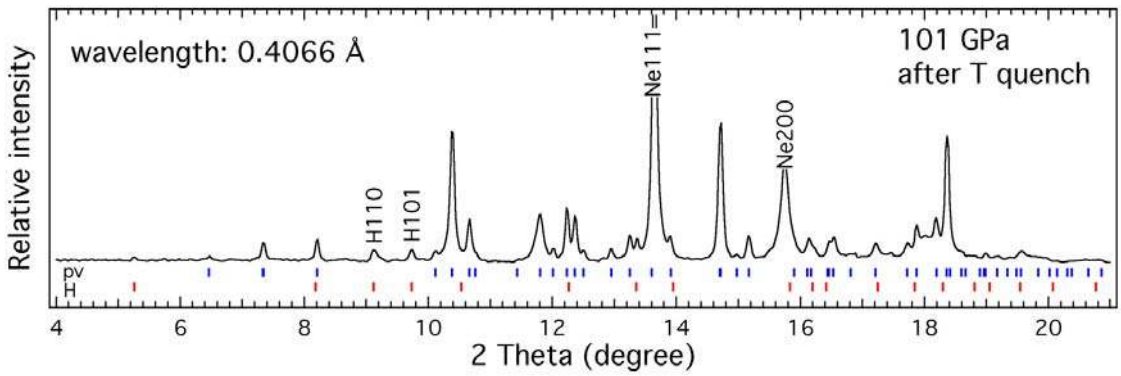

Fig. S9 XRD pattern of run products of Fs15 composition in a Ne medium. Minor H phase is observed in a pv dominant diffraction pattern at 101 GPa after *T* quench to 300 K from heating at 2250 K.

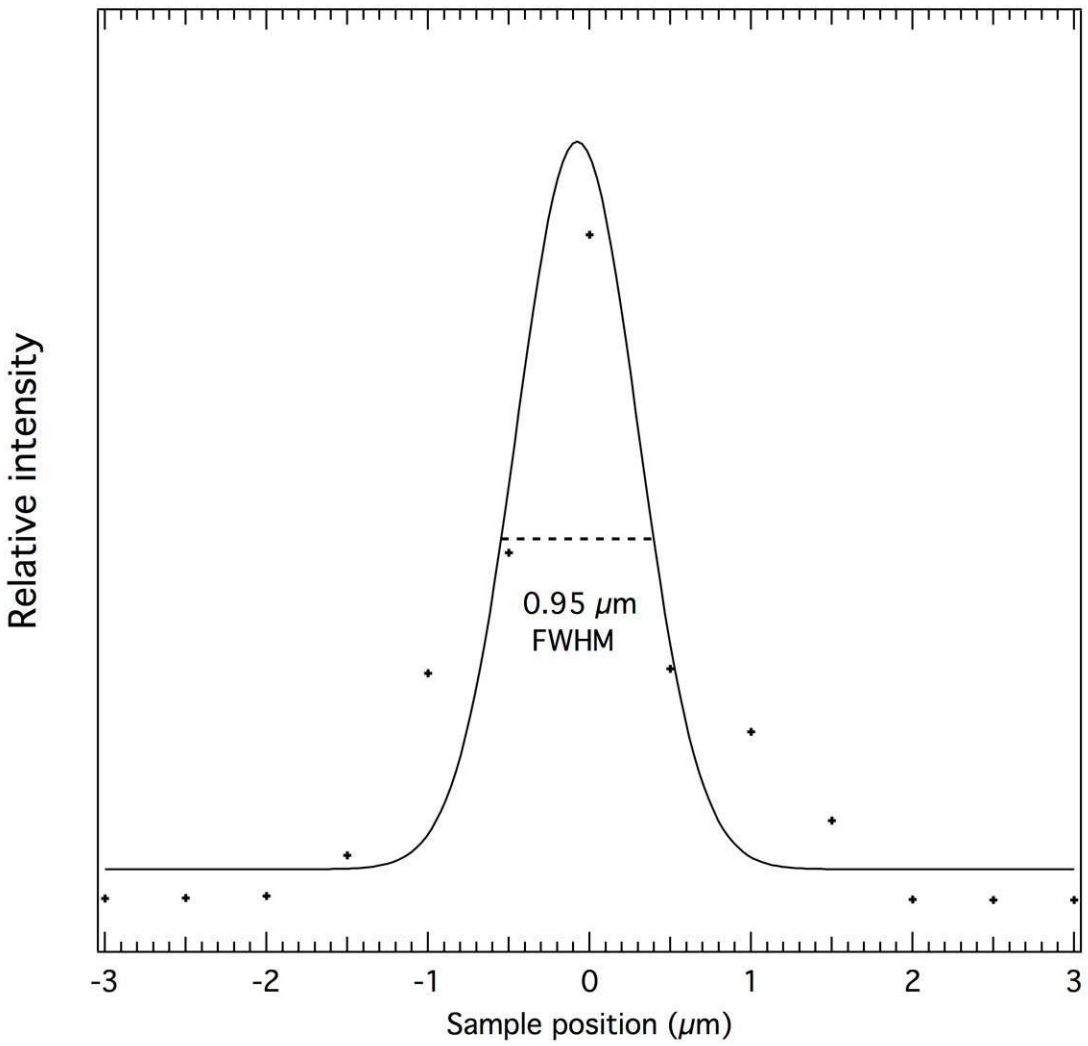

Fig. S10 X-ray mapping of crystallite grain size at 101 GPa. Intensity of one of diffraction spots is plotted as function of sample position measured with ~500 nm x-ray beam. The crystal size is determined to be ~0.5 μm after deconvolution.

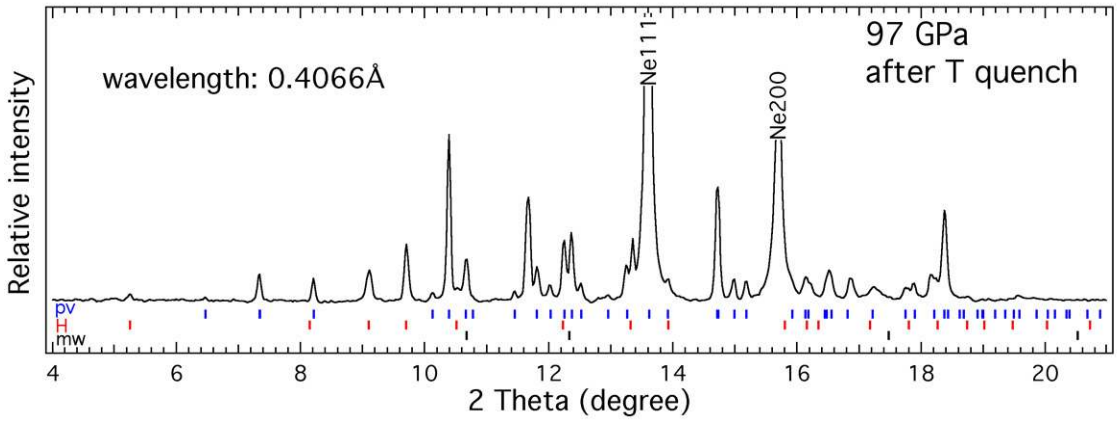

Fig. S11 H-phase formed in an fp saturated environment. The starting composition has a composition of $MgO:FeO:SiO_2$ = 0.86:0.19:1.0 ($(Mg,Fe)SiO_3$:(Mg,Fe)O =100:5). The XRD pattern is collected when the sample was quenched to room T after heated at 2300 K and 97 GPa (x-ray wavelength: 0.4066 Å). The calculated peak positions of the pv, H and mw phases are shown by small ticks.

Table S1. Single-crystal XRD of one of the crystallites of the H phase. The unit cell parameters: a = 5.096(2) Å, c = 2.862(3) Å; $\alpha = \beta = 90°$, $\gamma = 120°$ (x-ray beam wavelength of 0.3738 Å) at 101 GPa with Fs15 starting composition. The Bragg angle 2θ, rotation angle ω and azimuthal angle η are calculated from the orientation matrix and observed as XRD spots. Intensities are normalized to the strongest peak which is set to 100.

B	H	K	L	2θ (°)	ω (°)	η (°)	d (Å)	Intensity
	-1	0	1	8.93	-1.3	63.4	2.395	69
	-1	1	1	8.93	-16.2	32.8	2.395	86
	0	1	-1	8.93	-11.4	268.8	2.401	81
	1	-1	-1	8.95	0.3	212.8	2.399	100
	1	0	-1	8.95	8.7	243.2	2.402	63
	-1	-1	1	11.29	3.0	87.4	1.897	5.5
	1	1	-1	11.27	14.3	267.3	1.902	3.3
	-2	2	1	12.3	12.1	22.1	1.741	60
	0	-2	1	12.27	-12.4	105.9	1.746	54
	0	2	-1	12.25	0.3	285.7	1.751	82
	-1	-2	1	14.92	3.9	101.7	1.436	51
	1	0	-2	15.82	-4.1	240.6	1.358	8.6
	-2	1	2	17.28	-12.4	47.6	1.242	19
	-1	-1	2	17.29	-15.6	75.8	1.242	15
	1	1	-2	17.22	2.3	255.7	1.248	23
	2	-1	-2	17.25	11.0	227.4	1.245	23
	-2	0	2	17.97	-6.5	63.1	1.194	4.4
	2	-2	-2	17.95	8.6	211.9	1.198	20
	2	0	-2	17.93	13.7	242.9	1.199	8.0
	-1	4	-1	19.04	0.5	304.4	1.129	16
	-1	-2	2	19.89	-12.1	88.0	1.082	6.4
	1	2	-2	19.79	7.8	267.9	1.087	7.2
	2	1	-2	19.81	16.8	256.4	1.086	5.0
	-3	2	2	19.88	-3.1	38.2	1.081	3.6
	0	-4	1	20.94	-8.4	120.3	1.029	5.6
	0	4	-1	20.82	15.6	300.1	1.033	11
	0	3	-2	20.92	0.4	278.7	1.030	5.1

Table S2. Single-crystal XRD data of one of the crystallites in the Al-bearing sample. The H phase has the unit cell: a = 5.109(4) Å, c = 2.845(1) Å; $\alpha = \beta = 90°$, $\gamma = 120°$ at 100 GPa, with $(Mg_{0.80}Fe_{0.20})(Al_{0.04}Si_{0.96})O_3$ opx starting composition (x-ray beam wavelength of 0.4066 Å). The Bragg angle 2θ, rotation angle ω and azimuthal angle η are calculated from the orientation matrix and observed as XRD spots. Intensities are normalized to the strongest peak which is set to 100.

H	K	L	2θ (°)	ω (°)	η (°)	*d* (Å)	Intensity
-1	0	0	5.268	11.35	128.99	4.424	24
1	0	0	5.264	18.06	308.57	4.428	26
0	-1	-1	9.750	1.56	54.63	2.393	49
0	1	1	9.743	13.53	234.55	2.394	42
1	0	1	9.741	-9.94	258.63	2.395	47
-1	1	1	9.752	11.95	203.22	2.392	67
1	-1	-1	9.750	-12.60	23.29	2.392	100
-2	0	0	10.547	8.16	129.07	2.212	8.4
-2	0	-1	13.361	-12.77	96.14	1.748	39
2	0	1	13.370	0.68	275.97	1.747	33
-3	1	0	13.956	-18.90	138.41	1.674	6.7
3	-1	0	13.969	1.94	318.09	1.672	8.9
-3	1	1	16.211	-2.04	165.79	1.442	33
3	-2	-1	16.220	-4.86	354.31	1.441	20
0	1	2	17.270	0.59	230.48	1.354	9.4
-1	-1	-2	18.828	-14.98	66.11	1.243	13
1	-2	-2	18.840	-9.99	38.31	1.242	16
1	1	2	18.835	5.63	245.96	1.243	11
-4	1	0	19.084	-15.1	136.73	1.226	7.3
0	-2	-2	19.572	-4.50	54.25	1.196	6.1

References and Notes

1. M. Murakami, K. Hirose, K. Kawamura, N. Sata, Y. Ohishi, Post-perovskite phase transition in $MgSiO_3$. *Science* **304**, 855–858 (2004). doi:10.1126/science.1095932

2. A. R. Oganov, S. Ono, Theoretical and experimental evidence for a post-perovskite phase of $MgSiO_3$ in Earth's D" layer. *Nature* **430**, 445–448 (2004). doi:10.1038/nature02701 Medline

3. T. Tsuchiya, J. Tsuchiya, K. Umemoto, R. M. Wentzcovitch, Phase transition in $MgSiO_3$ perovskite in the earth's lower mantle. *Earth Planet. Sci. Lett.* **224**, 241–248 (2004). doi:10.1016/j.epsl.2004.05.017

4. J. Badro, J. P. Rueff, G. Vankó, G. Monaco, G. Fiquet, F. Guyot, Electronic transitions in perovskite: Possible nonconvecting layers in the lower mantle. *Science* **305**, 383–386 (2004). doi:10.1126/science.1098840

5. J. Badro, G. Fiquet, F. Guyot, J. P. Rueff, V. V. Struzhkin, G. Vankó, G. Monaco, Iron partitioning in Earth's mantle: Toward a deep lower mantle discontinuity. *Science* **300**, 789–791 (2003). doi:10.1126/science.1081311

6. J. Li *et al*., Electronic spin state of iron in the Earth's lower mantle. *Proc. Natl. Acad. Sci. U.S.A.* **101**, 14027 (2004). doi:10.1073/pnas.0405804101 Medline

7. S. Stackhouse, The spin deep within. *Nat. Geosci.* **1**, 648–650 (2008). doi:10.1038/ngeo327

8. E. Ohtani, T. Sakai, Recent advances in the study of mantle phase transitions. *Phys. Earth Planet. Inter.* **170**, 240–247 (2008). doi:10.1016/j.pepi.2008.07.024

9. R. D. van der Hilst, H. Karason, Compositional heterogeneity in the bottom 1000 kilometers of Earth's mantle: Toward a hybrid convection model. *Science* **283**, 1885–1888 (1999). doi:10.1126/science.283.5409.1885

10. E. J. Garnero, A. K. McNamara, Structure and dynamics of Earth's lower mantle. *Science* **320**, 626–628 (2008). doi:10.1126/science.1148028

11. W. J. Su, R. L. Woodward, A. M. Dziewonski, Degree 12 model of shear velocity heterogeneity in the mantle. *J. Geophys. Res.* **99**, 6945 (1994). doi:10.1029/93JB03408

12. M. Murakami, Y. Ohishi, N. Hirao, K. Hirose, A perovskitic lower mantle inferred from high-pressure, high-temperature sound velocity data. *Nature* **485**, 90–94 (2012). doi:10.1038/nature11004 Medline

13. A. Ricolleau, Y. Fei, E. Cottrell, H. Watson, L. Deng, L. Zhang, G. Fiquet, A.-L. Auzende, M. Roskosz, G. Morard, V. Prakapenka, Density profile of pyrolite under the lower mantle conditions. *Geophys. Res. Lett.* **36**, L06302 (2009). doi:10.1029/2008GL036759

14. Y. Fei, Y. Wang, L. W. Finger, Maximum solubility of FeO in (Mg, Fe)SiO_3-perovskite as a function of temperature at 26 GPa: Implication for FeO content in the lower mantle. *J. Geophys. Res.* **101**, 11525 (1996). doi:10.1029/96JB00408

15. Y. Tange, E. Takahashi, Y. Nishihara, K.-i. Funakoshi, N. Sata, Phase relations in the system MgO-FeO-$SiO_2$to 50 GPa and 2000°C: An application of experimental techniques using multianvil apparatus with sintered diamond anvils. *J. Geophys. Res.* **114**, B02214 (2009). doi:10.1029/2008JB005891

16. W. L. Mao, Y. Meng, G. Shen, V. B. Prakapenka, A. J. Campbell, D. L. Heinz, J. Shu, R. Caracas, R. E. Cohen, Y. Fei, R. J. Hemley, H. K. Mao, Iron-rich silicates in the Earth's D" layer. *Proc. Natl. Acad. Sci. U.S.A.* **102**, 9751–9753 (2005). doi:10.1073/pnas.0503737102 Medline

17. S. Tateno, K. Hirose, N. Sata, Y. Ohishi, Solubility of FeO in (Mg,Fe)SiO_3 perovskite and the post-perovskite phase transition. *Phys. Earth Planet. Inter.* **160**, 319–325 (2007). doi:10.1016/j.pepi.2006.11.010

18. J.-F. Lin, H. Watson, G. Vankó, E. E. Alp, V. B. Prakapenka, P. Dera, V. V. Struzhkin, A. Kubo, J. Zhao, C. McCammon, W. J. Evans, Intermediate-spin ferrous iron in lowermost mantle post-perovskite and perovskite. *Nat. Geosci.* **1**, 688–691 (2008). doi:10.1038/ngeo310

19. S. M. Dorfman, Y. Meng, V. B. Prakapenka, T. S. Duffy, Effects of Fe-enrichment on the equation of state and stability of (Mg,Fe)SiO_3 perovskite. *Earth Planet. Sci. Lett.* **361**, 249–257 (2013). doi:10.1016/j.epsl.2012.10.033

20. Materials and methods are available as supplementary materials on *Science* Online.

21. S. Lundin, K. Catalli, J. Santillán, S.-H. Shim, V. B. Prakapenka, M. Kunz, Y. Meng, Effect of Fe on the equation of state of mantle silicate perovskite over 1Mbar. *Phys. Earth Planet. Inter.* **168**, 97–102 (2008). doi:10.1016/j.pepi.2008.05.002

22. H. O. Sørensen, S. Schmidt, J. P. Wright, G. B. M. Vaughan, S. Techert, E. F. Garman, J. Oddershede, J. Davaasambuu, K. S. Paithankar, C. Gundlach, H. F. Poulsen, Multigrain crystallography. *Z. Kristallogr.* **227**, 63–78 (2012). doi:10.1524/zkri.2012.1438

23. L. Wang, Y. Ding, W. Yang, W. Liu, Z. Cai, J. Kung, J. Shu, R. J. Hemley, W. L. Mao, H. K. Mao, Nanoprobe measurements of materials at megabar pressures. *Proc. Natl. Acad. Sci. U.S.A.* **107**, 6140–6145 (2010). doi:10.1073/pnas.1001141107 Medline

24. Y. Fei, D. Virgo, B. O. Mysen, Y. Wang, H. K. Mao, Temperature-dependent electron delocalization in (Mg,Fe)SiO_3 perovskite. *Am. Mineral.* **79**, 826 (1994).

25. J. M. Jackson, J. M. Jackson, W. Sturhahn, G. Shen, J. Zhao, M. Y. Hu, D. Errandonea, J. D. Bass, Y. Fei, A synchrotron Mossbauer spectroscopy study of (Mg,Fe)SiO_3 perovskite up to 120 GPa. *Am. Mineral.* **90**, 199–205 (2005). doi:10.2138/am.2005.1633

26. R. Sinmyo, K. Hirose, S. Muto, Y. Ohishi, A. Yasuhara, The valence state and partitioning of iron in the Earth's lowermost mantle. *J. Geophys. Res.* **116**, B07205 (2011). doi:10.1029/2010JB008179

27. A. R. Hutko, T. Lay, J. Revenaugh, E. J. Garnero, Anticorrelated seismic velocity anomalies from post-perovskite in the lowermost mantle. *Science* **320**, 1070–1074 (2008). doi:10.1126/science.1155822

28. M. Panning, B. Romanowicz, Inferences on flow at the base of Earth's mantle based on seismic anisotropy. *Science* **303**, 351–353 (2004). doi:10.1126/science.1091524

29. D. J. Frost, C. A. McCammon, The redox state of Earth's mantle. *Annu. Rev. Earth Planet. Sci.* **36**, 389–420 (2008). doi:10.1146/annurev.earth.36.031207.124322

30. A. Rohrbach, M. W. Schmidt, Redox freezing and melting in the Earth's deep mantle resulting from carbon-iron redox coupling. *Nature* **472**, 209–212 (2011). doi:10.1038/nature09899 Medline

31. Y. Fei, H.-K. Mao, B. O. Mysen, Experimental determination of element partitioning and calculation of phase relations in the MgO-FeO-SiO2 system at high pressure and high temperature. *J. Geophys. Res.* **96**, 2157 (1991). doi:10.1029/90JB02164

32. Y. Fei, A. Ricolleau, M. Frank, K. Mibe, G. Shen, V. Prakapenka, Toward an internally consistent pressure scale. *Proc. Natl. Acad. Sci. U.S.A.* **104**, 9182–9186 (2007). doi:10.1073/pnas.0609013104 Medline

33. A. Boultif, D. Louër, Powder pattern indexing with the dichotomy method. *J. Appl. Cryst.* **37**, 724–731 (2004). doi:10.1107/S0021889804014876

34. C. Nisr, G. Ribárik, T. Ungár, G. B. M. Vaughan, P. Cordier, S. Merkel, High resolution three-dimensional x-ray diffraction study of dislocations in grains of $MgGeO_3$ post-perovskite at 90 GPa. *J. Geophys. Res.* **117**, B03201 (2012). doi:10.1029/2011JB008401